Accepted by Tribology International as a research paper

Effects of solid viscoelasticity and loading rates on the squeeze film lubrication towards polymer-based materials: A numerical study

Xianjiu Lu[a*1], Kaiyue Jing[a], Xiangquan Wu[b], Qingen Meng[c], Zhongmin Jin[c,d,e*2]

[a] College of Mechanical and Electrical Engineering, Qingdao University, 308 Ningxia Road, Qingdao, Shandong, 266071, China
[b] School of Materials Science and Engineering, Xi’an University of Technology, Xi’an, Shaanxi, 710048, China
[c] School of Mechanical Engineering, University of Leeds, LS2 9JT, UK
[d] State Key Laboratory of Manufacturing System Engineering, School of Mechanical Engineering, Xi’an Jiaotong University, 99 Yanxiang Road, Xi’an, Shaanxi, 710054, China
[e] Tribology Research Institute, School of Mechanical Engineering, Southwest Jiaotong University, Chengdu, 610031, Sichuan, China

*1 Corresponding author:
Tel: 0086-18936418630
Email: xjlu@qdu.edu.cn
*2 Corresponding author:
Tel: 0086-13689289660
Email: zmjin@swjtu.edu.cn

Abstract

This study employs numerical simulations to investigate the effects of solid viscoelasticity and loading rates on the squeeze film lubrication performance. A novel generalized numerical lubrication model of point contact including a rigid sphere interacting with a viscoelastic semi-infinite plane is established. The Maxwell and Standard Linear Solid (SLS) models are adopted to describe the solid viscoelastic characteristics. By integrating the multigrid method (MG) with Fast Fourier Transform (FFT) algorithm, the viscoelastic squeeze film lubrication simulation was conducted. The proposed squeeze film lubrication model with SLS viscoelastic solid was applied to quantitatively analyze the time-dependent film thickness and pressure distributions in ultra-high-molecular-weight polyethylene (UHMWPE) hip joints. Results indicate that the initial squeeze-film stage requires a higher number of time step divisions, while the influence of time step partitioning weakens as squeeze time increases. A distinct secondary pressure equilibrium of the SLS model was exhibited after the initial squeeze stage, with minimum film thickness becoming significantly larger (up to 52% at 6τ) and central film thickness markedly greater (up to 51% at 6τ) than those predicted by a purely elastic model. Under high loading rates, instantaneous elasticity dominates, yielding higher pressures and film thicknesses, while low rates promote residual deformation, leading to wider contact areas and flatter pressure distributions. The unloading phase demonstrated lower peak pressures and a broader contact area compared to loading at the same load. The numerical framework provides an effective tool for analyzing transient squeeze-film lubrication performance in viscoelastic materials, offering insights for designing polymer-based lubricated systems.

Keywords: Viscoelasticity; Squeeze film lubrication; point contact; loading rates

1 Introduction

Viscoelastic materials, characterized by their time-dependent mechanical response, are extensively employed in a wide range of engineering and biomedical applications, such as tires, seals, rolling bearings [1] and biomedical implants [2]. Unlike purely elastic materials, which exhibit an instantaneous and fully recoverable deformation upon loading, viscoelastic materials display significant hysteresis due to their inherent structural complexity. This behavior cannot be adequately described by classical elastic contact mechanics. Instead, the time-dependent property can be described using different kinds of viscoelastic constitutive models such as Maxwell and standard linear solid (SLS) models. Among them, the Maxwell viscoelastic solid model is primarily used for simulating the deformation of soft thermoplastic plastics near their melting temperature (exhibiting strong viscoelastic properties). However, the Maxwell viscoelastic model is too simple to accurately capture the creep characteristics of polymers and similar materials. Consequently, more sophisticated models such as the SLS are frequently adopted to better characterize the viscoelastic properties of these materials.

Numerous studies have focused on dry contact involving solid viscoelastic properties. However, lubricants are often present between solid surfaces or need to be added to enhance the tribological performance of friction pairs. Proper lubrication can reduce adhesion and wear and extend the service life of soft materials such as polymers. Therefore, the solid viscoelastic properties and lubrication should be considered in combination to investigate their interaction mechanisms. Lubrication that takes into account the viscoelastic properties of solid materials is referred to as viscoelastic hydrodynamic lubrication (VEHL). Comparative analyses have revealed substantial deviations of the VEHL model from conventional elastohydrodynamic lubrication (EHL) frameworks, whether based on steady-state [3-11] or time-dependent conditions [12-20].

Elsharkawy [3] used the Newton-Raphson iterative method to solve the line contact viscoelastic hydrodynamic lubrication problem. Hooke and Huang [4] employed the multigrid method to examine the impact of solid viscoelastic properties on line contact viscoelastic hydrodynamic lubrication. Putignano and Dini [7] applied the BEM method to solve the viscoelastic hydrodynamic lubrication problem between a rigid sphere and a viscoelastic semi-infinite plane, investigating the influence of viscoelastic properties on lubrication. Building on this model, Putignano [11, 17] further studied the effects of solid viscoelasticity on viscoelastic hydrodynamic lubrication for different contact pairs, such as hard on soft, soft on hard, and soft on soft. Yan Zhao [8, 21] developed a computational method for viscoelastic deformation of a semi-infinite plane in point contact and applied it within the multigrid method to construct a point contact viscoelastic hydrodynamic lubrication model, studying the effects of solid viscoelasticity on fluid film pressure and thickness distribution. He et al. [14] developed a VEHL model to examine how imperfect viscoelastic-elastic interfaces affect lubrication, demonstrating that interface defects, layer thickness, and modulus ratio markedly influence film thickness and pressure profiles. Li et al. [18] developed a semi-analytical VEHL model for polymer composites with non-uniform reinforcements, showing that reinforcement properties, shape, and position markedly affect contact pressure and film thickness.

The aforementioned studies on viscoelastic lubrication were all conducted under steady-state lubrication contact conditions. However, significant differences arise when considering the non-stationary lubrication conditions, particularly the pure squeeze viscoelastic lubrication conditions. Rohde et al. [22], Yoo [12] and Kaneko [13] developed a viscoelastic pure squeeze lubrication model for a rigid cylinder and a viscoelastic semi-infinite plane and conducted numerical solutions, finding that the film thickness in viscoelastic lubrication is different from that in pure elastic cases. Mustafa et al. [23, 24] conducted a numerical model for an oscillating squeeze film lubrication between a rubber and rigid surface and investigated the effects of permeability and roughness of the rubber surface on the hydrodynamic force and the leakage flow rate in the squeeze film. Recently, Putignano [19] constructed a viscoelastic line contact pure squeeze lubrication model for a rigid cylinder and a viscoelastic semi-infinite plane, solving the Reynolds equation using the finite difference method and solid deformation using the Boundary Element Method. The results showed that, unlike classical elastohydrodynamic lubrication, fluid pressure and film thickness depend on the viscoelastic relaxation of the solid material, with peaks occurring at the edges of the lubrication contact area, emphasizing the necessity of considering solid viscoelasticity in lubrication.

In addition to the VEHL in line and cylindrical contacts, in engineering applications, many practical problems such as polymer-based artificial joints and rolling bearings can be simplified to a squeeze film lubrication model including a rigid spherical indenter and a semi-infinite viscoelastic solid plane. Sahasranaman et al. [25, 26] proposed a non-iterative numerical method for VEHL in point contact and solved the relaxation problem including a rigid spherical indenter rapidly makes contact with a viscoelastic substrate lubricated by a liquid film. Except for the relaxation problem of squeeze film lubrication, many practical applications can be simplified as squeeze film lubrication in point contact under constant load such as soft artificial joints, seals and ball bearings et al. However, numerical simulation of constant loaded squeeze film lubrication in point contact considering solid viscoelasticity remains limited. Additionally, due to the time-dependent property of Viscoelastic materials, the deformation of present time instant is determined by the present and historical loading profiles. It has been indicated by Chen et al. [27] that the loading rate has great influences on the viscoelastic dry contact performance. However, the influences of loading rates on the viscoelastic squeeze film behavior remains unclear.

By integrating established methodologies including the MG method, FFT algorithm and linear viscoelastic constitutive models (Maxwell and SLS), a novel computational framework has been developed to model the transient viscoelastic squeeze-film lubrication of point contact. In contrast to the classical EHL theory, the time-dependent deformation (stress relaxation and creep) of the solid is considered. A more realistic simulation of the squeeze-film lubrication behavior in soft material contacts has been implemented. The underlying physical mechanisms have been elucidated through investigating the interaction between the viscoelastic relaxation-induced surface recovery and transient squeeze-film flow effects. The accuracy of the proposed model and numerical method was indirectly validated through comparison with the dry contact simulation results. Furthermore, the SLS viscoelastic models are adopted to more accurately describe the complex viscoelastic behavior of UHMWPE hip joints. Based on this model, the effects of loading rate on squeeze-film lubrication performance were systematically investigated, with particular emphasis on the viscoelastic characteristics of UHMWPE in prosthetic applications. This analysis provides mechanistic sight into how loading conditions influence pressure distribution, film thickness and the transition between elastic-dominated and viscoelastic-dominated response regimes in polymer-based lubricated systems.

2 Materials and methods

2.1 Model description

The squeeze film lubrication behavior under conditions of pure normal approach motion was investigated in the present study. This scenario is highly relevant in numerous engineering applications. For example, it appears during the initial or final stages of impact loading or reciprocating motion, where the formulation and sustenance of the lubricating film are predominantly governed by the squeeze effect between the surfaces. Under this specific condition, the generation of hydrodynamic pressure primarily stems from the time-dependent variation in film thickness, known as the squeeze film motion.

To characterize the indentation contact between a rigid sphere and a viscoelastic half space, a ball on plane configuration is adopted as the fundamental geometrical model in this study (Figure 1). Through equivalent treatment in terms of elastic modulus and geometry, this sphere-plane model can be widely applied to the lubrication analysis of artificial hip and knee joints, as well as polymer rolling bearings.

2.2 Viscoelastic squeeze film lubrication equations

Since squeeze film motion was incorporated into the study, the time-dependent Reynolds equation [28] was applied to characterize the system's transient response.

$$\frac{\partial}{\partial x}\left(\frac{h^3}{12\eta}\frac{\partial p}{\partial x}\right)+\frac{\partial}{\partial y}\left(\frac{h^3}{12\eta}\frac{\partial p}{\partial y}\right)=\frac{\partial h}{\partial t} \tag{1}$$

where the term $\partial h/\partial t$ denotes the squeeze film motion, while p represents the hydrodynamic pressure and η signifies the lubricant viscosity. The formulation of this equation rests upon the classical assumptions of lubrication theory, wherein the lubricant flow is considered laminar. Due to the viscoelastic response effects, the pressure is too low to affect either the viscosity or density for the soft contact problem [4, 19]. Therefore, the fluid is modeled as an isoviscous and incompressible Newtonian fluid, and the no-slip boundary condition is applied at the solid-fluid interfaces. Furthermore, owing to the extremely thin film geometry, the pressure is assumed to be constant across the film thickness, and the effects of inertial and body forces are neglected. A critical simplification adopted in the current model is the isothermal assumption, which neglects thermal effects and associated viscosity variations induced by viscous shear within the squeeze film.

The film thickness [8], h, comprises the undeformed geometrical gap and the viscoelastic deformation, which can be formulated as follows

$$h(x,y,t) = h_{00}(t) + \frac{x^2}{2R} + \frac{y^2}{2R} + \delta(t) \tag{2}$$

where $h_{00}(t)$ represents the rigid displacement, R denotes the equivalent radius along x and y directions, e.g., for the artificial hip joint with radial clearance c, the equivalent radius can be calculated as $R = (R_h(R_h+c))/c$, R_h is the radius of the rigid femoral head, $\delta(t)$ accounts for the time-dependent viscoelastic deformation.

The external load applied to the rigid ball was balanced by the resultant force produced by the film pressure

$$\int\int\int \mathrm{p}(x,y,t)\,dxdydt = w(t) \tag{3}$$

2.3 Viscoelastic constitutive relation and Boltzmann principle

The detailed theory of viscoelasticity of has been introduced in the previous studies [16, 29]. Briefly, based on the framework of linear viscoelasticity and small strain assumptions, the stress-strain relationship is described by the Boltzmann superposition principle in the present study. This principle states that the strain of the material at present time t is the superposition of the effects of all historical stress applications. Each stress increment applied at a previous moment ξ contributes to the current strain, determined by the material's creep compliance $\Phi(t-\xi)$ over the time interval $t-\xi$. The time-dependent strain $\varepsilon(t)$ can be obtained by the creep compliance $\Phi(t-\xi)$ [19] and Boltzmann hereditary integral [27, 30]

$$\varepsilon(t) = \int_0^t \Phi(t-\xi)\frac{d\sigma}{d\xi}d\xi \tag{4}$$

For the Maxwell viscoelastic model as shown in Figure 2(a), the creep compliance function [27] is

$$\Phi_{cm}(t) = \frac{1-v^2}{E}\left(1 + \frac{t}{\tau}\right) \tag{5}$$

where, E represents the storage modulus and v the Poisson's ratio, and τ the relaxation time, η/E. The Maxwell viscoelastic model is relatively too simple to capture the relaxation and creep behaviors of polymer based materials [27]. Therefore, the further complex viscoelastic model such as SLS model (Figure 2(b)) is used to describe the time-dependent deformation behaviors of such materials. For the standard linear viscoelastic model, the creep compliance function [27] is

$$\Phi_{cs}(t) = \frac{1}{E_2}\left[1 + \frac{E_2}{E_1}\left(1 - e^{-\frac{t}{\tau}}\right)\right] \tag{6}$$

where, E_2 represents the storage modulus and E_1 the loss modulus, and τ the relaxation time.

2.4 Computational framework for viscoelastic deformation

Based on the semi-infinite half-space approximation and linear elasticity assumption, the Boussinesq integral [31] has been widely used to calculate the normal displacement of the contact surfaces for the elastic point contact between a rigid ball and an elastic half space

$$\delta(x,y) = \frac{1-v^2}{\pi E}\int\int \frac{p(x\prime,y\prime)}{\sqrt{(x-x')^2+(y-y')^2}}dx'dy' \tag{7}$$

Similar to the time-dependent strain calculation in Section 3.1, for the system consisting of a rigid ball and a viscoelastic half space, the viscoelastic deformation can be determined by substituting the elastic compliance $(1-\upsilon^2)/E$ in equation (7) with the viscoelastic compliance operator $\Phi_c(t)$[4]. It should be noted that the viscoelastic compliance operator $\Phi_c(t)$ refers to the general conceptual variables such as Maxwell and SLS viscoelastic models. Combine with Boltzmann hereditary integration, the viscoelastic deformation can be calculated as follows

$$\delta(x,y,t)=\int_0^t \frac{\Phi_c(t-\xi)}{\pi}\int\int \frac{1}{\sqrt{(x-x')^2+(y-y')^2}}\frac{\partial p(x\prime,y\prime,\xi)}{\partial \xi}dx'dy'd\xi \tag{8}$$

The non-dimensional form can be written as

$$\overline{\delta}(X,Y,T)=\lambda_1\int_0^T \overline{\Phi}_c\left(T-\overline{\xi}\right)\int\int \frac{1}{\sqrt{(X-X')^2+(Y-Y')^2}}\frac{\partial P\left(X',Y',\overline{\xi}\right)}{\partial \overline{\xi}}dX'dY'd\overline{\xi} \tag{9}$$

where, $\lambda_1=\frac{2p_H R_x}{\pi E' a}$.

In order to perform numerical calculations, it is necessary to discretize the continuous space-time and pressure history into grids and steps, respectively. The pressure distributions were assumed as constant in each time step. On each grid level, the pressure at node (k, l) at γ^{th} time instant was denoted as $P_{\text{k,l,}\gamma}$, then the pressure increment in the γ^{th} step was $P_{\text{k,l,}\gamma}$-$P_{\text{k,l,}\gamma\text{-1}}$. The discretized viscoelastic deformation at node (i,j) at γ^{th} time instant can be written as

$$\overline{\delta}_{i,j,\gamma}=\lambda_1\sum_{\gamma'=1}^{\gamma}\left\{\overline{\Phi}_c(\gamma-\gamma')\left[\sum_{k=0}^{n_x}\sum_{l=0}^{n_y}D_{|i-k|,|j-l|}\left(P_{k,l,\gamma\prime}-P_{k,l,\gamma\prime-1}\right)\right]\right\} \tag{10}$$

where, $D_{|i-k|,|j-l|}$ is the elastic deformation coefficient matrix.

It can be seen from equation (10) that the elastic deformation at initial time instant can be calculated as a discrete convolution of initial pressure distributions and instantaneous elastic deformation coefficients. The effects of previous pressure distributions of adjacent time instant on the present time instant were considered by the Boltzmann hereditary integral principle. The elastic deformation at γ time instant is a convolution of elastic deformation coefficients and pressure increment of γ^{th} time instant and adjacent previous $(\gamma\text{-}1)^{\text{th}}$ time instant. The discrete convolution was calculated using the 2-based decimation-in-frequency FFT algorithm, which can significantly improve the efficiency of convolution operation. With the developed numerical algorithms, the viscoelastic deformation under arbitrary loading conditions can be calculated efficiently as long as the viscoelastic compliance operator is determined whatever the material is linear or nonlinear.

2.5 Numerical algorithm and implementation

This section details the numerical framework developed to solve the coupled viscoelastic squeeze film lubrication problem. The algorithm integrates a MG method for efficient solution of the transient Reynolds equation, a FFT-accelerated convolution scheme for calculating surface deformations, and the Boltzmann hereditary integral to account for viscoelastic material memory effects. A rigorous convergence criterion based on error norms ensures the reliability of the numerical solutions.

To enhance numerical stability and facilitate the analysis of scaling effects, the governing equations were first non-dimensionalized. The Reynolds equation for pure squeeze motion in a point contact configuration was then discretized on a uniform spatial grid. At k^{th} grid level, the domain is discretized into $(n_x^k+1)\times(n_x^k+1)$ nodes. The densest grid on the finest level used in this study has dimensions $N_x\times N_y$ along x and y directions. A second-order central difference scheme was applied to the pressure-induced Poiseuille flow terms, and a first-order backward difference scheme was used for the transient squeeze flow term.

Gauss-Seidal point relaxation iteration method was used to solve the discrete non-dimensional Reynolds equation at each level of the grids. Different from the Finite Difference Method for the line contact Reynolds equation, which is effective for 1D problems. Applying a simple FDM to the 2D point contact equation would be prohibitively slow and may fail to converge for the fine meshes required to resolve the high pressure gradients. The slow convergence of low-frequency error components after grid refinement is a well-known limitation of traditional iterative methods. To overcome this fundamental limitation, the MG method was employed.

The main advantage of the MG method lies in its hierarchical approach to error correction. High-frequency errors are efficiently smoothed by a small number of iterations on the fine grid, while low-frequency errors are effectively corrected on the coarse grid. This process is recursive, dramatically accelerating the overall convergence rate to nearly grid-independent efficiency.

In the current study, a Full Approximation Scheme (FAS) was implemented within the MG framework. Its core concept lies in solving an equation on the coarse grid that incorporates not only the residual from the fine grid but also the solution information inherent to the coarse grid itself. This ensures consistency in the overall approximation between the coarse and fine grids. A 3-level W-cycle strategy was employed in the present study. The explanation of single W-cycle has been detailed in the previous research [32].

A grid convergence study was conducted using three grid densities (129×129, 257×257 and 513×513). The relative difference in key output parameters was less than 3% between the 257×257 and 513×513 grids, indicating sufficient numerical convergence was achieved at the 257×257 density. Consequently, this grid size was adopted for all simulations. On each grid level, the second-order central difference method was used to the pressure induced flow terms and first-order backward difference to the right squeeze induced flow term.

On each grid level, the discrete convolution was solved to calculate the elastic deformation and FFT algorithm was used to facilitate this calculation process. The detailed information towards the application of FFT algorithm on the calculation of discrete convolution can be illustrated as follows: Firstly, zero-padding is applied to the pressure and influence coefficients to convert linear convolution into circular convolution. Secondly, FFT is used to transform the zero-padded sequences into the frequency domain. Thirdly, the complex spectra of the pressure and influence coefficients are multiplied pointwise in the frequency domain. Fourthly, an Inverse FFT (IFFT) is performed to transform the product back to the spatial domain. Finally, the elastic deformation in the physical domain is obtained by truncating the first $N_x\times N_y$ points from the IFFT result. This combination was particularly advantageous for point contact, which drastically reduces the computational cost of the convolution integral from $O(N_x^2 \times N_y^2)$ to $O((N_x \times N_y)\log(N_x \times N_y))$ for a $N_x \times N_y$ grid. Combined with the Boltzmann hereditary integral, the viscoelastic deformation can be calculated for all the time instants during the whole squeeze film process. The rigid displacement constant h_{00} was adjusted using the external load and integration of pressure distributions. The detailed technical routine that combined the MG method and viscoelastic deformation algorithm is illustrated in Figure 3.

The pressure relaxation iteration was regarded as convergence when the accumulated pressure relative differences between adjacent iterations. The relative pressure differences calculation formula and criterion can be given as follows

$$Err_p = \frac{\sum_{i=0}^{N_x}\sum_{j=0}^{N_y}\left|\tilde{P}_{i,j}-\bar{P}_{i,j}\right|}{\sum_{i=0}^{N_x}\sum_{j=0}^{N_y}\tilde{P}_{i,j}} < 1 \times 10^{-7} \tag{11}$$

The relative error between the integrated squeeze film pressure within the contact area and the externally applied load can be calculated by the following formula

$$Err_w = \frac{\sum_{i=0}^{N_x}\sum_{j=0}^{N_y}\tilde{P}_{i,j}-\bar{W}}{\bar{W}} < 1 \times 10^{-5} \tag{12}$$

where, $\bar{W}$ is the dimensionless applied external load.

A rigorous mesh sensitivity analysis requires quantitative evaluation based on error norms. Among these, the L_2 norm is widely adopted due to its ability to reflect the global error over the entire computational domain. For time-dependent minimum film thickness, central film thickness, and maximum pressure ($u(t)$), the error can be defined as:

$$Err_u = \frac{\left|u_{\Delta t}-u_{\Delta tref}\right|_{L_2}}{\left|u_{\Delta tref}\right|_{L_2}} \tag{13}$$

where, $u_{\Delta tref}$ denotes the reference solution obtained with a finer time step of 600, which is regarded as being closer to the true solution. In this study, a relative L_2 error of 5% is adopted as the threshold for temporal convergence of the numerical solution. The solution is considered converged when the error is at or below this value.

2.6 Model validation

To ensure the reliability and accuracy of the proposed viscoelastic squeeze film lubrication model of point contact, systematic model validation and numerical verification procedure were implemented. The approaches aimed to assess the model's capability in capturing the core physical mechanisms, guaranteeing the stability of the numerical solution, and ensuring the reproducibility of the results.

The validity of the current computational results was verified by comparing them with the corresponding dry contact calculation results. In order to validate the current lubrication model and related numerical method, the pressure and film thickness distributions were expressed in dimensionless form and direct comparisons of pressure distributions with the dry contact calculation results were conducted. The verification confirms that the selected operating condition parameters are consistent with the dry contact calculation conditions used by Chen et al. [27]. This parameter selection ensures that the computational results can be directly compared and validated against related analytical and numerical studies.

A typical feature of VEHL is the strong coupling between the transient fluid flow and the time-dependent, historical-sensitive deformation of the viscoelastic solid. The viscoelastic deformation at any given instant is intrinsically dependent on the entire loading history, making the accuracy of the numerical solution highly sensitive to the temporal discretization density. To analyze this temporal grid sensitivity, the total squeeze time was discretized into a range of 20 to 600 time steps.

Furthermore, to verify the numerical stability of the implemented Boltzmann hereditary integral algorithm, which plays an important role in the calculation of the time-dependent viscoelastic deformation, a dedicated convergence test was also conducted. The viscoelastic deformation at a specific time instant ($t = 2\tau$) was calculated using a series of mesh densities ranging from 25 to 600 time steps.

Similarly, the sufficiency of the spatial computational domain was verified. The primary simulations employed a domain from -2 to 2 (in dimensionless coordinates) in both the x and y directions. To confirm that this domain size is adequate to capture the essential physics of the squeeze film lubrication without being influenced by artificial boundary effects, a comparative simulation was performed using a significantly larger domain (-4 to 4 in both directions).

2.7 Computational conditions for UHMWPE hip joint analyses

The computational parameters for this study on UHMWPE hip joints were selected based on established literature [29, 33] concerning joint biomechanics and implant performance. Varied loads from 300 N to 3000 N were adopted, with a femoral head radius of 0.014 m and a radial clearance of 1×10^{-4} m. The material's viscoelastic properties, namely the relaxation time (τ) and the mechanical loss factor (defined as the ratio of loss and storage modulus, E_1/E_2), were chosen corresponding to the normal human body temperature of 37°C [34]. To comprehensively capture the time-dependent material response including creep, stress relaxation and recovery, which is crucial for analyzing rate-sensitive behavior, the SLS viscoelastic model was employed for the investigations detailed in section 3.4.

To simulate dynamic physiological loading, conditions of different loading rates particular three gait patterns were implemented. Based on reported gait cycle durations ranging from 0.59 s to 1.33 s for activities such as slow walking, normal walking and slow running [35], corresponding loading rates of 2407 N/s, 5538 N/s and 9562 N/s were applied. A broader parametric study was also conducted by simulating continuous loading rates corresponding to cycles from 0.1 s to 1.5 s. This approach was designed to reveal the effect of loading rate on viscoelastic squeeze film lubrication performance. To ensure that observed differences were stemmed solely from the loading physics and not from numerical artifacts, a uniform time step ($\Delta T = 0.0056$) was used for all the loading rate cases. It is important to note that for all these cyclic loading simulations, the final maximum load reached in each case was consistent at 3000 N, differing only in the rate at which this load was applied. The specific geometric and material parameters employed herein are referenced from typical designs of UHMWPE artificial hip joints, with details provided in Table 1.

3 Results

3.1 Spatiotemporal mesh sensitivity analysis

Figure 4 presents the dimensionless minimum/central film thickness, maximum pressure and relative L_2 error across different number of time step discretization within a squeeze period (2τ). As the number of time steps increases, the relative L_2 errors of the minimum/central film thickness and maximum pressure show a monotonically decreasing trend. When the time steps increase from 20 to 200, the error decreases rapidly. When the number of time steps reaches 200, the errors in the minimum film thickness, central film thickness, and maximum pressure all fall below 5%, satisfying the convergence criterion. At the 0.5τ time instant, the numerical analysis revealed significant differences in key parameters: the minimum film thickness shows substantial variations of 53.9% between cases with 20 and 600 time steps, gradually decreasing to 9.2% for 100 steps, 5.2% for 160 steps, and 3.8% for 200 steps. Parallel trends were observed in central film thickness, with relative differences of 42%, 7.6%, 4.3%, and 3.2% for the same number of time steps, respectively. Maximum pressure values exhibited remarkable consistency, with relative differences of merely 3.1% between 20 and 600 steps and 0.49% for 100 steps. The comparative analysis at subsequent time instants (τ and 2τ) revealed markedly reduced relative differences between cases. Specifically, the minimum film thickness showed variations of only 2.5% and 1.6% between 200 and 600 steps at τ and 2τ, respectively, while the maximum pressure demonstrated negligible differences of 0.002%. It can be seen that increasing temporal resolution significantly enhanced the stability and accuracy of film thickness and pressure calculations, particularly during the critical initial stage of the squeeze period (0.5τ). The influence of time step discretization became progressively less pronounced at later stages (τ and 2τ). The temporal pattern suggested that accurate numerical modeling requires higher time step resolution primarily during the early phase of the squeeze period, while coarser discretization may be sufficient during later stages without compromising computational accuracy.

Figure 5 illustrates the impact of computational domain size on the evolution of both the minimum/central film thickness and the maximum pressure throughout the simulated squeeze process. The results from the two tested domain sizes exhibit excellent agreement for both film thickness and pressure profiles, confirming that a computational domain spanning from -2 to 2 in both the x and y directions is adequate to capture the essential physics of the squeeze film lubrication phenomenon across the entire simulated duration.

Figure 6 further investigates the sensitivity of the numerical solution to temporal discretization by presenting the viscoelastic deformation at the specific time instant of 2τ under different time step sizes. Notably, the maximum discrepancy between the results obtained with the coarsest (25 steps) and finest (600 steps) temporal discretization is less than 0.02%. The negligible difference demonstrates the excellent numerical stability of the adopted Boltzmann hereditary integral algorithm with the present chosen time step of 200, ensuring the reliability of the time-dependent deformation predictions.

3.2 The squeeze film lubrication of Maxwell viscoelastic model

Figure 7(a) presents the evolution of dimensionless maximum pressure for both the purely elastic and Maxwell viscoelastic models during the squeeze-film lubrication process. Figure 7(b) provides a comparative analysis of the dimensionless pressure distributions from the present squeeze-film lubrication model against established dry-contact pressure solutions by Radok and Lee [36] and Chen et al. [27] at specific time instants (0.5τ, τ, and 2τ). The overall pressure profiles predicted by the lubrication model show excellent agreement with the dry-contact solutions across these time points. Notably, the peak pressure location for both conditions shifts to the edge of the contact region by $t = 2\tau$. The primary discrepancy arises in the exit region of the contact area, where the squeeze-film pressure exhibits a gradual decay to ambient conditions, a feature absent in the dry-contact models where pressure terminates abruptly. This gradual pressure relief at the outlet is a characteristic dictated by fluid flow dynamics in lubrication. The strong correlation demonstrated in Figure 7(b) validates that the current viscoelastic squeeze-film lubrication model accurately captures the pressure distribution evolution across a wide range of time scales, effectively bridging the behavior between instantaneous elastic contact and time-dependent viscoelastic response under lubricated conditions.

In addition to the pressure distributions, the film thickness evolution for both purely elastic and viscoelastic (Maxwell model) squeeze-film lubrication was analyzed. Figure 8 illustrates the dimensionless minimum and central film thicknesses during the process. Initially, the film thicknesses for both material models were nearly identical. However, as the squeeze motion progressed, a distinct divergence emerged: the decay rate of the minimum film thickness for the Maxwell model began to exceed that of the elastic model, and this difference gradually widened over time. Concurrently, the central film thickness for the viscoelastic Maxwell model became and remained thicker than that of the elastic counterpart shortly after motion onset, with the disparity also increasing as the process continued.

Figure 9 shows the temporal evolution of dimensionless pressure and film thickness distributions along the entrainment direction (y=0). During the squeeze-film process, the pressure distribution of the elastic model resembled the Hertzian contact, with the lubricated contact area remaining relatively constant over time. The film thickness decreased rapidly initially and then more slowly, becoming progressively flatter as the motion proceeds. In contrast to the elastic model, the overall pressure distribution of the Maxwell model was significantly smaller, and the contact area was much larger. Notably, the pressure peak gradually decreased in magnitude and shifted towards the edge regions of the contact, resulting in a distinctive "double-peak" distribution. Furthermore, the overall film thickness of the Maxwell model was thinner at the edges of the contact zone but thicker in the central region compared to the elastic model. As the squeeze motion continued, the film thickness in the central region gradually decreased while local peaks formed near the contact edges, as shown in Figure 9.

3.3 The squeeze film lubrication of SLS viscoelastic model

Figure 10 (a) presents the temporal evolution of the dimensionless maximum pressure for the purely elastic and SLS viscoelastic models during the pure squeeze-film lubrication process. For the elastic model, the dimensionless maximum pressure rapidly increases to a peak and stabilizes at a value approximating unity. In contrast, the maximum pressure for the SLS model exhibits a distinct viscoelastic relaxation response: after an initial rise, it undergoes a gradual decay, eventually tending to stabilize at a significantly lower value of approximately 0.63. This divergence underscores the fundamental difference between instantaneous elastic recovery and time-dependent stress relaxation inherent to viscoelastic materials. Figure 10 (b) shows the cross-sectional profiles of the dimensionless pressure distribution for both lubricated and dry contact conditions at selected time instants ($t = 0.5\tau$, 1.0τ, and 2.0τ). A key observation is that the pressure distributions under lubricated and dry contact conditions are remarkably similar across the central contact region, conforming to expectations from classical Hertzian contact theory where lubricant pressures in the contact zone can approximate dry contact stresses. The primary distinction emerges in the exit regions of the lubricated contact. Here, the hydrodynamic lubrication pressure does not terminate abruptly but rather decays gradually to ambient conditions, following the characteristic behavior dictated by the Reynolds equation. This smooth decay at the outlet is a critical feature of fluid film lubrication that prevents pressure discontinuities and influences load capacity. The comparative analysis highlights how the introduction of a lubricant film modifies the pressure field at the contact boundaries while maintaining a similar core pressure distribution, a factor essential for accurate modeling of mixed or full-film lubrication regimes.

Figure 11 shows the evolution of dimensionless minimum and central film thicknesses for the purely elastic and SLS viscoelastic models during the squeeze-film lubrication process. The initial dimensionless minimum film thicknesses for both the elastic and SLS models were nearly identical at the onset of squeeze motion. A critical crossover point is observed at a dimensionless time of $t = 1.28\tau$, where the minimum film thickness of the SLS model begins to consistently exceed that of the elastic model. At this precise moment, both models share an identical minimum film thickness value of 0.00658. Following this crossover, the evolution of the minimum film thickness for the SLS model diverges markedly from that of the purely elastic (and Maxwell) model. As the squeeze process continues, the minimum film thickness for the SLS model not only overtakes but sustains a growing advantage over the elastic case. This disparity progressively amplifies, culminating in a substantial 52% difference by $t = 6\tau$. Quantitatively, at this final time instant, the dimensionless minimum film thickness is 0.00254 for the elastic model compared to 0.00386 for the SLS model. A similar, yet more pronounced trend is evident for the central film thickness. The central film thickness for the SLS model is generally greater than that of the elastic model shortly after the squeeze motion begins, and this difference also enlarges over time. By $t = 6\tau$, the central film thickness for the SLS model (0.00865) is 51% larger than that of the purely elastic model (0.00574).

Figure 12(a) shows the evolution of dimensionless rigid displacements for the purely elastic and SLS viscoelastic models during the squeeze-film lubrication process. The rigid displacement for both models rapidly decreases to approximately -0.9 within a very short initial period ($t < 0.04\tau$). Subsequently, the elastic model displacement stabilizes around -0.996, whereas the SLS model displacement continues to decrease, eventually reaching a value of approximately -1.58. This divergence highlights the pronounced time-dependent, creep-dominated deformation characteristic of the viscoelastic material, which is absent in the purely elastic response. Figure 12(b) shows the dimensionless deformation profiles for the elastic and SLS models at selected time instants (t = 0.5τ, 1.0τ, 2.0τ, 3.0τ, 4.0τ, 6.0τ). The viscoelastic deformation increment progressively diminishes as the squeeze motion proceeds, indicating that the material's time-dependent response gradually approaches a steady state. Notably, the relative difference in maximum deformation between t = 4.0τ and t = 6.0τ is merely 0.5%, suggesting that the deformation evolution becomes nearly negligible beyond t = 4.0τ for the given conditions. This observation underscores the critical role of the material's relaxation time (τ) in governing the transient deformation kinetics during squeeze-film lubrication.

Figure 13 shows temporal evolution of the cross-sectional dimensionless pressure and film thickness profiles for the purely elastic and SLS viscoelastic models, as simulated by the present squeeze-film lubrication model. During the squeeze process, the pressure distribution for the elastic model closely resembles the classic Hertzian contact profile, with the lubricated contact area remaining relatively constant over time. Correspondingly, the film thickness for the elastic case decreases rapidly initially, followed by a more gradual decline, and the profile becomes progressively flatter as the motion proceeds. In contrast, the pressure distribution for the SLS model is significantly lower in magnitude and spread over a much larger contact area compared to the elastic case. The film thickness in the central constriction region of the SLS contact is initially smaller than that of the elastic model at early times (e.g., t = 0.5τ and 1.0τ). However, as the squeeze process continues, the overall film thickness profile along the x-direction for the SLS model eventually becomes greater than that of the purely elastic case. Throughout the entire squeeze duration, the contact area for the SLS model remains substantially larger than that for the elastic model, highlighting the profound influence of solid viscoelasticity on transient lubrication mechanics.

3.4 Effects of loading rates on the VEHL performance of UHMWPE hip joints

The key lubrication performance parameters (including maximum pressure, minimum film thickness, central film thickness and rigid displacement) under a load of 3000 N are quantitatively summarized for the three investigated loading rates in Table 2. When the loading rate decreases from 9562 N/s to 2407 N/s, the maximum pressure decreases by approximately 24.0%, the minimum film thickness decreases by about 57.4%, the central film thickness decreases by about 41.3%, while the rigid displacement increases by about 24.1%. These systematic variations highlight the significant influence of loading rate on viscoelastic squeeze-film lubrication behavior, with lower rates promoting greater material compliance and flattened pressure distributions, ultimately leading to reduced film thickness and expanded contact area.

Figure 14 shows the dimensionless maximum squeeze-film pressure as a function of external load for UHMWPE hip joints during the loading phase under three different loading rates (2407 N/s, 5538 N/s, and 9562 N/s). For all three loading rates, the pressure initially increased to a peak value before undergoing a subsequent gradual decrease as the squeeze-film motion progressed. Notably, the initial peak values of the dimensionless maximum pressure were remarkably similar across the different loading rates. However, following this initial peak, the pressure evolution began to diverge significantly based on the loading rate. The most pronounced decrease in maximum fluid pressure was observed at the slowest loading rate of 2407 N/s. The pressure decline was less severe at the intermediate rate of 5538 N/s, and the least decrease occurred at the fastest rate of 9562 N/s. This demonstrates a clear inverse relationship between the loading rate and the magnitude of pressure decay after the initial peak. By the time the final peak load of 3000 N was reached, the dimensionless maximum pressures had stabilized at distinct final values: 0.69772 for 2407 N/s, 0.85494 for 5538 N/s, and 0.91792 for 9562 N/s. This quantitative result underscores the significant influence of loading rate on the steady-state pressure distribution within the viscoelastic squeeze film, with higher loading rates preserving a greater proportion of the initial peak pressure.

Figure 15 shows the dimensionless rigid displacement as a function of external load for UHMWPE hip joints under different loading rates. The results for the three loading rates (2407 N/s, 5538 N/s and 9562 N/s) exhibit a trend of gradual convergence with increasing load. Notably, the overall rigid displacement is highest for the fastest loading rate (9562 N/s), followed by the intermediate rate (5538 N/s), and is lowest for the slowest rate (2407 N/s). Figure 16 illustrates the dimensionless minimum and central film thickness with external load for UHMWPE hip joints under three different loading rates. During the loading phase (from 300 N to 3000 N), both the minimum and central film thicknesses demonstrate a clear dependence on loading rate: the film thickness values are greatest for the highest loading rate (9562 N/s), intermediate for 5538 N/s, and smallest for the lowest rate (2407 N/s).

Figure 17 shows the cross-sectional pressure distributions along the *x* direction under a constant load of 1650 N for different loading rates during the loading and unloading phases. A clear dependence of the pressure profile on the loading rate is observed. For both loading and unloading, the pressure distribution exhibits its flattest profile at the slowest loading rate of 2407 N/s. Correspondingly, the contact area is largest at this rate, followed by 5538 N/s and 9562 N/s, indicating a transition from a viscoelasticity-dominated to an elasticity-dominated response with increasing loading rate. Furthermore, under the same load of 1650 N, the peak pressure during the unloading phase is notably lower, while the contact area is broader compared to the loading phase, highlighting the path-dependent and hysteretic behavior of the viscoelastic material. Figure 18 shows the cross-sectional film thickness distributions along the *x* direction under a constant external load of 1650 N for different loading rates during the loading and unloading phases. Consistent with the pressure results, the film thickness profile is also flattest at the slowest loading rate of 2407 N/s. The overall film thickness values in this case are smaller than those observed at the higher rates of 5538 N/s and 9562 N/s. This trend aligns with the enlarged contact area observed in Figure 17, where lubricant is distributed over a wider region, resulting in a thinner film on average.

Figure 19 illustrates the influence of varying loading time (corresponding to continuous loading rates) from 300 N to 3000 N on the maximum pressure and rigid displacement during a squeeze film lubrication process. As the loading time increases, the maximum squeeze film pressure generated upon reaching 3000 N correspondingly decreases.

Concurrently, the rigid displacement increases with prolonged loading time. However, the growth rate gradually decelerates. Figure 20 shows the effect of varying loading cycles (0.1 s to 1.5 s) on both the minimum and central film thicknesses. It can be observed that both the minimum and central film thicknesses decrease as the loading time increases. Furthermore, the rate of this decrease gradually diminishes with loading times.

4 Discussions

A novel viscoelastic squeeze film lubrication model is proposed specifically formulated for point contact scenarios, which are characterized by a finite, typically elliptical contact area. Unlike the infinite line contact problem, a more complex, two dimensional pressure and film thickness distributions are involved in the point contact conditions, which is also significantly influenced by lateral side leakage of the lubricant. Accurately capturing these phenomena is therefore essential for simulating a wide range of real-world engineering components where the contact area is inherently finite. Key applications include artificial hip and knee joints, polymer rolling bearings, and gear contacts operating under misalignment or at the ends of teeth, where the contact geometry deviates from an ideal line. Therefore, a corresponding computational algorithm tailored for polymer-based materials was implemented. The related governing equations were solved to obtain full numerical lubrication solutions for two typical viscoelastic constitutive models: Maxwell and SLS models. The validity of the proposed model and numerical scheme was established through a rigorous verification process. In details, the computed squeeze film pressure distributions were compared against analytical and numerical dry contact solutions. Different temporal discretization densities were used to verify the accurate numerical lubrication modeling and Boltzmann integral numerical stability. Excellent agreement between the present numerical solution and the analytical and numerical dry contact solutions indirectly validated the proposed model and algorithms. Based on the developed viscoelastic squeeze film lubrication model, different loading modes particularly the three gait patterns were adopted to investigate the effects of loading rates on the viscoelastic squeeze film lubrication performance.

The calculation of viscoelastic deformation in this study is founded upon the Boltzmann superposition principle, which constitutes the cornerstone of linear viscoelastic theory under the assumption of small strains. The principle posits that the strain response of a material at any given time is a linear superposition of the effects of its entire loading history. The adopted framework is computationally efficient and provides excellent accuracy for scenarios where deformation remain within the material's linear response regime, a condition satisfied during the early and intermediate stages of the squeeze process investigated here. In the present numerical implementation for squeeze film lubrication, the viscoelastic deformation at each computational time step is computed by incorporating the complete loading history from the simulation's inception. The material's intrinsic memory effect was fully captured without employing a truncated time window. Consequently, the accuracy of accumulated deformation, and the predicted pressure and film thickness, becomes inherently sensitive to the density of the temporal grid discretization.

A comprehensive temporal grid sensitive analysis was conducted to critically assess the discretization requirements for accurately resolving the lubrication simulation within a squeeze cycle. The analysis revealed pronounced sensitivity of the film thicknesses to temporal resolution, particularly during the initial compression phase (Figure 4). This stage is characterized by rapid transients, where steep gradients in fluid flow and surface deformation demand high temporal resolution to achieve physical fidelity. Coarser discretization during this phase introduced significant deviations in both the minimum and central film thicknesses. In contrast to film thickness, the maximum pressure values exhibited robust consistency across discretization levels (Figure 4). This suggests that the pressure distribution within the contact stabilizes more rapidly and is less susceptible to variations in temporal resolution once the initial transient has passed. The observed convergence patterns carry significant implications for computational strategy. At the later stages of the squeeze process (e.g., at dimensionless times τ and 2τ), variations in both film thickness and pressure with further time-step refinement became negligible. It is suggested that computational efficiency can be substantially enhanced by employing adaptive time-stepping strategies. A finer temporal resolution should be concentrated during the initial rapid transients, while coarser steps can be adopted as the system evolves toward a quasi-steady state. Such an approach would optimally balance numerical accuracy with computational resource expenditure. The calculated viscoelastic deformation at 2τ serves to validate the numerical stability of the implemented Boltzmann hereditary integral algorithm within the examined range of discretization. The successful verification underpins the reliability of the subsequent simulations investigating the effects of viscoelastic model and loading rates.

The Maxwell and SLS model were integrated into a pure squeeze film lubrication framework to analyze the transient response of viscoelastic materials under normal approach motion. The simulations revealed that both the film thickness and pressure distribution during the squeeze process exhibited pronounced time-dependent evolution and stress relaxation effects, which are typical features of viscoelastic behavior. This behavior stands in fundamental contrast to the assumptions of classical EHL theory, which typically treats the contacting solids as purely elastic, thereby neglecting the material’s memory and rate-dependent response. The accuracy and predictive capability of the proposed viscoelastic squeeze film lubrication model were rigorously validated. A direct comparison was made between the pressure distributions predicted by the present model and established reference solutions, including the analytical solutions of Radok and Lee [36] as well as the numerical solution of Chen et al. [27] (Figures 7 and 10). The results demonstrated excellent agreement within the central contact region for both the Maxwell and SLS model implementations.

Upon the application of an instantaneous load, both the Maxwell and SLS viscoelastic models initially exhibit a response identical to that of a purely elastic material, characterized by the immediate deformation of the spring element and the generation of instantaneous elastic strain. It is consistent with the fundamental behavior of linear viscoelastic models under suddenly applied loads, where an instantaneous elastic response is always present. The evolution of the pressure distribution diverges significantly from the classical elastic Hertzian solution due to the intrinsic time-dependent nature of viscoelasticity.

In the Maxwell model, it is characterized by the development of a double-peak pressure profile (Figures 7(b) and 9(a)). The formulation of this distribution can be attributed to a complex, dynamic interplay among three key mechanisms: viscoelastic stress relaxation, transient fluid squeeze flow, and the resulting time-evolving surface deformation. The process can be detailed as follows: A Hertzian-like pressure peak was induced firstly as the application of instantaneous load, which is governed by the spring's immediate elastic response. Subsequently, the dashpot in series introduces a critical time delay in the load transfer and stress redistribution within the material. This delay initially suppresses the full development of material deformation, leading to an overall pressure magnitude lower than that predicted by a purely elastic model for the same nominal load. As the process evolves, viscoelastic stress relaxation becomes the dominant mechanism. The relaxation of the dashpot components leads to a rapid decay of stress, and consequently pressure, at the center of the contact zone where the initial stress concentration was highest. Concurrently, transient fluid dynamics play a decisive role. The delayed deformation response of the viscoelastic solid, coupled with the extrusion of fluid from the converging gap, acts to redistribute and concentrate the pressure towards the peripheral regions of the contacts. In the edge regions, the initial stress state is lower, allowing the viscoelastic relaxation process to reach completion more rapidly. This facilitated a partial recovery of the elastic deformation due to the viscoelastic effect. This localized elastic recovery induced increase in local film thickness, creating a more favorable geometry for pressure generation. The observed phenomenon is consistent with the temporal evolution of viscoelastic pressure distributions reported in the literature [19].

For the SLS model, the mechanical behavior is described by a spring in parallel with a Maxwell unit (Figure 2(b)). During the initial loading phase of the squeeze process, the rapid fluid extrusion from the converging gap dominates the film thickness reduction for both the purely elastic and SLS viscoelastic models. Since the instantaneous elastic response of both materials is similar, their initial film thickness decay rates are comparable (Figure 11). As time progresses under constant load, the viscous dashpot within the SLS model begins to relax. The stress relaxation allows material to undergo time-dependent creep, redistributing the internal stress. Crucially, this process gradually releases a portion of the elastic energy stored in the spring elements. Due to this relaxation behavior, a time-delayed surface recovery effect manifests during the ongoing squeeze process. When the fluid is extruded and the film thickness decreases, the surface of the SLS solid does not passively maintain its deformation. Instead, driven by internal stress relaxation, it exhibits a tendency to recover its original shape. This recovery motion opposes the approach of the two surfaces, thereby effectively slowing the decay rate of the film thickness. As the film becomes thinner, the fluid extrusion rate decelerates, while the cumulative effect of viscoelastic deformation recovery becomes increasingly significant. Eventually, a transient balance is reached between these two competing effects. As the squeeze film motion continues, the influence of viscoelastic recovery begins to surpass that of fluid extrusion, resulting in a film thickness under the SLS model that is notably greater than that predicted by the purely elastic model. In contrast, the purely elastic model, lacking such an intrinsic recovery mechanism, exhibits a more pronounced decay in film thickness.

A critical observation from the simulations is that the maximum dimensionless squeeze film pressure in the SLS model stabilizes at an asymptotic value of approximately 0.63 (Figure 10). This stabilization is not arbitrary but arises from the intrinsic viscoelastic relaxation characteristics of the SLS material and its dynamic coupling with the transient fluid squeeze flow. When the material parameters satisfy $E_1/E_2=1$, the ratio of the equilibrium modulus E_0 $(E_1E_2/(E_1+E_2))$ to the instantaneous elastic modulus E_2 is theoretically 0.5. In the present investigated spherical contact configurations, the maximum pressure $P_{\max}$ scales with the effective elastic modulus as $P_{\max} \propto E^{2/3}$ according to Hertz theory. Consequently, the ratio between steady-state pressure and initial pressure can be expressed as $P_{\max}(\infty)/P_{\max}(0) \approx (E_0/E_2)^{2/3} \approx 0.63$. Due to the weakening of fluid pressure as the film thins, the final support is determined by the equilibrium elastic deformation of the solid. Therefore, the dimensionless squeeze film pressure tends towards the dry contact maximum pressure (0.63) in the final equilibrium state (Figure 10). When the squeeze time exceeded three times the relaxation time, the viscoelastic material underwent significant relaxation, its viscoelastic effects gradually diminished, the final support is determined by the equilibrium elastic deformation of the solid and the squeeze film pressure and contact radius approached the asymptotic values (Figure 10) determined by two springs connected in series.

The selection of an appropriate constitutive model is crucial for accurately capturing the time-dependent mechanical response of polymers under dynamic loading. Although both the Maxwell and SLS models are functional in linear viscoelasticity, they exhibit distinct capabilities in simulating real material behaviors. The Maxwell model, characterized by a spring and dashpot in series, is inherently limited in its ability to accurately represent the creep and recovery behaviors typical of polymeric solids, as it predicts unlimited creep strain under constant stress. In contrast, the SLS model, which incorporates an additional spring in parallel with a Maxwell unit, provides a more comprehensive framework. It can effectively describe not only stress relaxation but also the bounded creep and eventual recovery observed in cross-linked polymers and many engineering thermoplastics. This makes the SLS model particularly suitable for simulating materials like UHMWPE, where long-term dimensional stability under load is critical, such as in artificial joint applications.

Prior experimental and theoretical studies [33] have confirmed that under the specific load of 300 N to 3000 N, the initial deformation response of UHMWPE can be well approximated by a linear elastic assumption. The primary objective of the present numerical model is to elucidate the fundamental time-dependent interplay between viscoelastic stress relaxations within the solid and the transient squeeze flow of the lubricant. For this purpose, a linear viscoelastic framework, as embodied by the SLS model, serves as a well-established and valid starting point, balancing physical fidelity with computational tractability. Consequently, the SLS model was adopted in this study to systematically characterize the influence of varying loading rates on the squeeze film lubrication performance of UHMWPE. A key finding from comparing the lubrication characteristics of UHMWPE hip joints under different loading rates was the loading rate independent nature of the initial peak pressure (Figure 14). This phenomenon occurred because the initial instantaneous load was identical in all numerical tests, despite the divergent differences determined by different loading rates. However, as the loading process continued, the evolution of the pressure field and film thickness became markedly rate-sensitive. Divergences in the transient response became apparent under different loading rates once the external load began to increase (Figure 17). By the time the instantaneous load reached 1650 N, the pressure distributions for the three representative loading rates (simulating slow walking, normal walking, and running gaits) were distinctly different. At this stage, the transient viscoelastic response became dominant, meaning the material's deformation became highly sensitive to the rate at which the load was applied. A general trend observed was that larger squeeze film pressures were sustained under higher loading rates (Figures 17 and 18). This can be attributed to the material exhibiting a more elastic-dominated response at high rates. The viscous dashpot in the SLS model has insufficient time to relax and accommodate the rapidly applied strain, leading to higher transient stresses within the solid and, consequently, higher fluid pressures. Conversely, at lower loading rates, viscoelastic effects become pronounced. The dashpot has adequate time to relax, leading to significant stress decay and time-dependent creep deformation. This results in a larger residual indentation depth, an enlarged contact area, and consequently, a flatter and more distributed pressure profile.

To further investigate these mechanisms, 15 groups of loading times corresponding to a continuous spectrum of loading rates were analyzed (Figures 19 and 20). The results conclusively demonstrate that the viscoelastic material exhibits stronger apparent contact resistance at higher loading rates. This finding aligns perfectly with previous dry-contact numerical analyses by Chen et al. [27], which reported similar rate-dependent pressure evolution. The interplay between the loading rate and the material’s intrinsic relaxation time determines whether the contact response is predominantly elastic (high rates) or viscoelastic (low rates), which in turn governs the pressure distribution, film thickness, and load-bearing capacity throughout the loading cycle.

Notably, during the loading phase, when the viscoelastic material was subjected to compression, the instantaneous elastic modulus dominated the response in a short period, leading to higher pressure peaks concentrated in the central contact area (similar to Hertz contact). During the unloading phase, the relaxation time of the base material was relatively long, and compared to the loading phase, the base material began to recover its deformation. However, the viscous resistance caused the recovery process to lag, preventing rapid elastic rebound, which resulted in an enlarged contact area and a dispersed pressure distribution.

Although valuable insights into the viscoelastic squeeze film lubrication mechanism were provided by the present study, it is important to acknowledge the inherent limitations, which stem from necessary simplifications adopted. The current model incorporates several key simplifications related to several aspects such as surface topography, fluid rheology and thermal effects. First, the contacting surfaces are assumed to be perfectly smooth. In practical engineering and biological applications, such as artificial joints or engineered bearings, surface roughness at the micrometer scale is ubiquitous and can be comparable to the lubricant film thickness value. This roughness can fundamentally alter the soft lubrication regime, potentially triggering a transition from full-film to mixed lubrication [37] or even boundary lubrication. Therefore, extending the current framework to incorporate measured or statistically representative surface roughness is a crucial next step to enhance model fidelity for real-world applications. Second, the lubricant is modeled as an isoviscous and incompressible Newtonian fluid. The Barus or Roelands viscosity-pressure relationship and fluid compressibility should be integrated into future models to accurately capture the piezo viscous effects that significantly influence pressure generation and load-bearing capacity in high pressure contacts. Third, the analysis is conducted under an isothermal assumption, neglecting heat generation due to viscous shear within the fluid and energy dissipation within the viscoelastic solid. This simplification was strategically employed to focus on the fundamental coupling between viscoelastic deformation and transient fluid flow. However, in scenarios involving high loading rates or cyclic loading, significant self-heating effects can occur within viscoelastic materials. This temperature rise can, in turn, alter the material's mechanical properties [15] such as an increase in temperature typically leads to a decrease in the elastic modulus and a shortening of relaxation times for polymers like UHMWPE. A fully coupled thermo-visco-elastohydrodynamic analysis represents a critical and complex future direction to understand performance under more severe operating conditions.

The model validation in this study relied on a rigorous numerical comparison with dry viscoelastic contact solutions. While this is a necessary first step, direct experimental validation of the transient lubricated squeeze-film process remains essential. Currently, there is a notable lack of publicly available high-fidelity experimental data for viscoelastic squeeze-film lubrication under conditions matching our simulations. Future work will aim to bridge this gap by employing advanced experimental techniques such as optical interferometry, a well-established method for in-situ measurement of thin lubricating films with high spatial and temporal resolution.

The current model is built upon the framework of linear viscoelasticity theory. This is appropriate for the moderate deformations and effectively captures the core relaxation and flow dynamics. However, for polymer-based materials like UHMWPE subjected to very large strains or long-term creep, geometric nonlinearities arising from finite deformations can become significant. In such cases, the changing contact geometry under large strain can profoundly influence contact mechanics and pressure distribution, and the stress-strain relationship itself becomes nonlinear. Building upon the present work, a logical and important extension is to incorporate geometric nonlinearity and develop a finite deformation viscoelastic constitutive model. This would involve conducting related finite strain measurements to inform the model formulation, ultimately leading to a more generalized framework capable of predicting the behavior of soft materials under extreme loading conditions.

The current full-history integration approach is computationally manageable for the cases presented (with up to 600 time steps), exploring very low loading rates would necessitate a large number of steps to maintain accuracy. To enable efficient studies across decades of loading rates, the implementation of a loading history truncation method coupled with an adaptive time-stepping algorithm is proposed. Such an algorithm would dynamically coarsen the temporal resolution during quasi-steady periods and refine it during rapid transients. A corresponding sensitivity analysis of the truncation length will be indispensable to rigorously balance computational efficiency with numerical accuracy, ensuring reliable results across the entire parameter space.

5 Conclusions

The current numerical study systematically reveals the significant impact of the viscoelastic properties of polymer materials on their squeeze film lubrication characteristics. Based on the Maxwell and SLS viscoelastic models, combined with the MG and FFT algorithm, the influence of the material's viscoelastic properties on squeeze film pressure and film thickness distributions during the squeeze process, as well as the characteristics under different loading rates, has been elucidated. The main conclusions are as follows:

1. The selection of time step size has a significant impact on the numerical calculation accuracy of lubrication, especially during the initial stage of squeeze. Increasing the number of time steps can effectively reduce the numerical error of the transient response in the initial stage and have little effect during the relaxation stage. This provides a theoretical basis for adopting an adaptive time step strategy (refining the step size in the initial stage and coarsening it in the later stage) to balance computational efficiency and accuracy. For the viscoelastic (SLS modeled materials) squeeze film problems investigated in this work, a time step of 200 is recommended to maintain a relative L_2 error below 5% while ensuring computational efficiency.
2. The squeeze film pressure distributions of the Maxwell and SLS viscoelastic models show a high degree of consistency with the dry contact pressure distributions. The consistency between lubricated and dry contact pressures provides a critical validation of our deformation solver. This agreement is expected when fluid effects become secondary to the solids' viscoelastic response, establishing the dry contact solution as a rigorous benchmark.
3. At the initial squeeze film stage, the squeeze film pressure and film thickness of Maxwell and SLS models were similar with that of the elastic model. After the initial squeeze film stage, the maximum pressure reaches a secondary equilibrium state for the SLS model from the time instant around 2τ. The minimum film thickness of SLS viscoelastic model was larger than the elastic model from time instant of 1.28τ, and the difference expanded to 52% at time instant of 6τ. The central film thickness of SLS was generally larger than the elastic model from the squeeze film motion processed, and the maximum difference expanded to 51% at time instant of 6τ.
4. At high loading rates, the material exhibits predominantly instantaneous elastic behavior, resulting in a larger overall pressure and thicker lubrication film in the contact zone. Under low loading rates, the presence of residual deformation on the viscoelastic solid surface leads to an expanded contact area and a flatter pressure distribution. Under the same load, the unloading phase exhibits lower peak pressures and a wider contact

area compared to the loading phase, which is due to the longer relaxation time experienced by the matrix material during unloading, resulting in greater viscoelastic deformation.

Author Contributions: Conceptualization, X.L. and Z.J.; methodology, X.L.; formal analysis, X.L. and Q.M.; investigation, X.L., K.J. and X.W.; resources, Z.J.; writing—original draft preparation, X.L.; writing—review and editing, Q.M.; visualization, X.L., K.J. and X.W.; supervision, Q.M. and Z.J.; project administration, X.L.; funding acquisition, X.L. and Z.J.

Funding: This research was funded by National Science Foundation of China, grants number 52035012, and Natural Science Foundation of Shandong Province, China, grants number ZR2023QE277.

References

[1] Santeramo M, Putignano C, Vorlaufer G, Krenn S, Carbone G. On the role of viscoelasticity in polymer rolling element bearings: Load distribution and hysteretic losses. Mechanism and Machine Theory. 2023;189.

[2] Wang D, de Boer G, Neville A, Ghanbarzadeh A. A Review on Modelling of Viscoelastic Contact Problems. Lubricants. 2022;10.

[3] Abdallah AA. Visco-elastohydrodynamic lubrication of line contacts. wear. 1996;199:45-53.

[4] Hooke C, Huang P. Elastohydrodynamic lubrication of soft viscoelastic materials in line contact. Proceedings of the Institution of Mechanical Engineers, Part J: Journal of Engineering Tribology. 1997;211:185-94.

[5] Hooke CJ. Elastohydrodynamic Lubrication of Soft Solids. 1997;32:185-97.

[6] Scaraggi M, Persson B. Theory of viscoelastic lubrication. Tribology International. 2014;72:118-30.

[7] Putignano C, Dini D. Soft Matter Lubrication: Does Solid Viscoelasticity Matter? ACS applied materials & interfaces. 2017;9:42287-95.

[8] Zhao Y, Liu HC, Morales-Espejel GE, Venner CH. Effects of solid viscoelasticity on elastohydrodynamic lubrication of point contacts. Tribology International. 2022;171.

[9] Michele Santeramo GC, Georg Vorlaufer, Stefan Krenn, Carmine Putignano. Viscohydrodynamic lubrication in conformal contacts: A numerical approach. International Journal of Solids and Structures. 2025;311.

[10] Wang L, Xiang G, Han Y, Yang T, Zhou G, Wang J. A mixed visco-hyperelastic hydrodynamic lubrication model for water-lubricated rubber bearings. International Journal of Mechanical Sciences. 2025;286.

[11] Putignano C. Soft lubrication: A generalized numerical methodology. Journal of the Mechanics and Physics of Solids. 2020;134.

[12] Yoo H. Some Effects of Viscoelastic Matrix on the Squeeze Films. A S L E Transactions. 1987;30:403-8.

[13] Kaneko S, Tanaka T. A Study on Squeeze Films Between Porous Rubber Surface and Rigid Surface: Analysis Based on the Viscoelastic Continuum Model. Journal of Tribology. 2004;126:719.

[14] He T, Wang QJ, Zhang X, Liu Y, Li Z, Kim HJ, et al. Visco-elastohydrodynamic lubrication of layered materials with imperfect layer-substrate interfaces. International Journal of Mechanical Sciences. 2021;189.

[15] He T WQJ, Zhang X, et al. Modeling thermal-visco-elastohydrodynamic lubrication (TVEHL) interfaces of polymer-based materials. Tribology International. 2021;154.

[16] Lu X, Meng Q, Jin Z. Effects of UHMWPE viscoelasticity on the squeeze-film lubrication of hip replacements. Biosurface and Biotribology. 2021;7:60-9.

[17] Putignano C. Oscillating viscoelastic periodic contacts: A numerical approach. International Journal of Mechanical Sciences. 2021;208.

[18] Li D, Zhu C, Wang A, He T. Modelling visco-elastohydrodynamic lubrication of polymer-based composites. Tribology International. 2022;174.

[19] Putignano C, Campanale A. Squeeze lubrication between soft solids: A numerical study. Tribology International. 2022;176.

[20] Zijia Wang JZ, Huailei Wang, Dan Guo, Koucheng Zuo, Zhiwei Mao. Visco-elastohydrodynamic lubrication and wear model amended by deformation velocity. International Journal of Mehcanical Sciences. 2024.

[21] Zhao Y, Morales-Espejel GE, Venner CH. Aspects of modeling and numerical simulation of dry point contacts between viscoelastic solids. Tribology International. 2022;165.

[22] Rohde S, Whicker D, Booker J. Elastohydrodynamic squeeze films: effects of viscoelasticity and fluctuating load. Journal of Lubrication Technology. 1979;101:74-80.

[23] Mustafa M, Chhanda NJ, Mahbubur Razzaque M. A numerical model of an oscillating squeeze film between a rubber surface and a rigid surface. Tribology International. 2010;43:202-9.

[24] Mahbubur RM, Mustafa M. Effects of permeability and surface roughness on the behavior of an oscillating viscoelastic squeeze film. Industrial Lubrication and Tribology. 2013;65:37-43.

[25] Sahasranaman A, Hui CY. A non-iterative numerical approach for visco-elasto-hydrodynamic lubrication problems. Extreme Mechanics Letters. 2025;74.

[26] A S. Analysis of lubricated normal contact of a rigid sphere on a viscoelastic halfspace. Cornell University. 2023.

[27] Chen WW, Wang JQ, Huan Z, et al. Semi-Analytical Viscoelastic Contact Modeling of Polymer-Based Materials. Journal of Tribology. 2011;133:041404.

[28] Bedewi M A A DD, Taylor C M. The squeeze-film lubrication of ellipsoids. Journal of Physics D: Applied Physics. 1992;21:A133.

[29] Lu X, Meng Q, Wang J, Jin Z. Transient viscoelastic lubrication analyses of UHMWPE hip replacements. Tribology International. 2018;128:271-8.

[30] Brinson H, Brinson L. Polymer engineering science and viscoelasticity: An Introduction. Springer, New York. 2008.

[31] Johnson KL. Contact mechanics. Cambridge university press. 1987.

[32] Venner CH. Multilevel solution of the EHL line and point contact problems. University of Twente. 1991.

[33] Jin ZM, Dowson D, Fisher J. An axisymmetric contact model of ultra high molecular weight polyethylene cups against metallic femoral heads for artificial hip joint replacements. Proceedings of the Institution of Mechanical Engineers, Part H: Journal of Engineering in Medicine. 1999;213:317-27.

[34] Deng M, Uhrich K. Viscoelastic behaviors of ultrahigh molecular weight polyethylene under three-point bending and indentation loading. Journal of biomaterials applications. 2010;24:713-32.

[35] Lu X, Liang M, Meng Q, Jin Z. Effects of Gait Patterns on the Viscoelastic Squeeze-Film Lubrication of Hip Replacements. Lubricants. 2025;13.

[36] Lee EH, Jens Rainer Maria Radok. The contact problem for viscoelastic bodies. Journal of Applied Mechanics. 1960;27:438-44.

[37] Masjedi M, Khonsari MM. Mixed lubrication of soft contacts: An engineering look. Proceedings of

the Institution of Mechanical Engineers, Part J: Journal of Engineering Tribology. 2017;231:263-73.

Table 1 Details of the lubrication conditions and computational parameters

Parameter	Values
Load, w/N	300-3000
Ball radius, R/m	0.014
Radial clearance, c/m	1.0×10^{-4}
Storage modulus, E_2/Pa	0.7×10^{9}
Loss modulus, E_1/Pa	0.7×10^{9}
Relaxation time, τ/s	13.81
Environment viscosity, η_0/Pa·s	0.01
Dimensionless computational domains	$-2 \le X \le 2$ and $-2 \le Y \le 2$
Grid density	256×256
Temporal steps	20-600

Table 2 Dimensionless maximum pressure, minimum and central film thicknesses, and rigid displacement at 3000 N obtained from different loading rates

Loading rate, λ(N/s)	Maximum pressure, $p_{\mathrm{max}}/p_{\mathrm{H}}$	Minimum film thickness, h_{min}/h_0	Central film thickness, h_{cen}/h_0	Rigid displacement, h_{00}
9562	0.91792	0.01353	0.02486	-1.0722
5538	0.85494	0.00992	0.01961	-1.1413
2407	0.69772	0.00577	0.01459	-1.3305

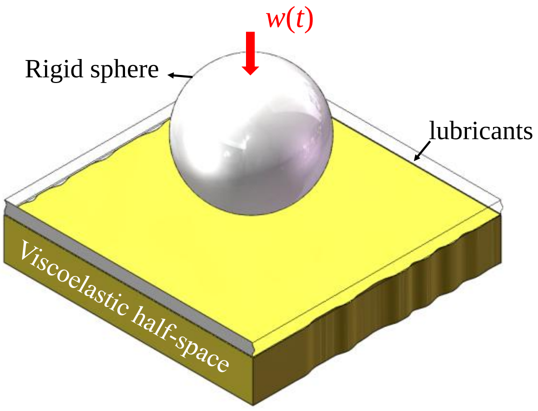

Figure 1 Squeeze film lubrication model of rigid ball and viscoelastic half space

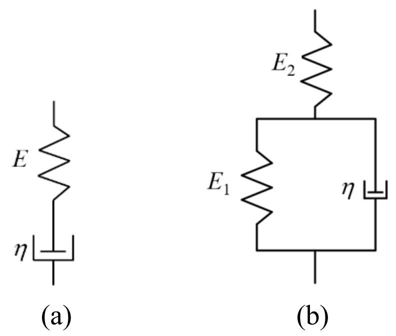

Figure 2 Maxwell (a) and SLS (b) models adopted in this study

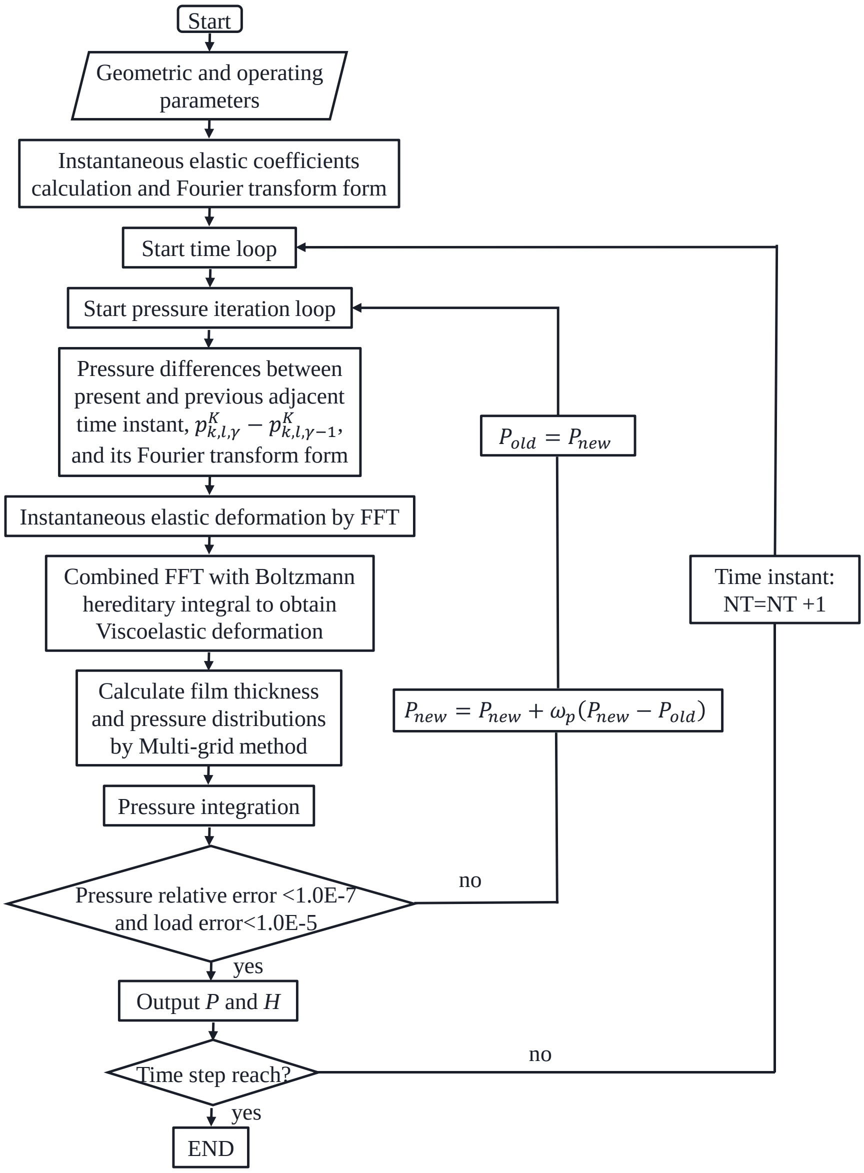

Figure 3 Calculation flow chart of viscoelastic squeeze film lubrication

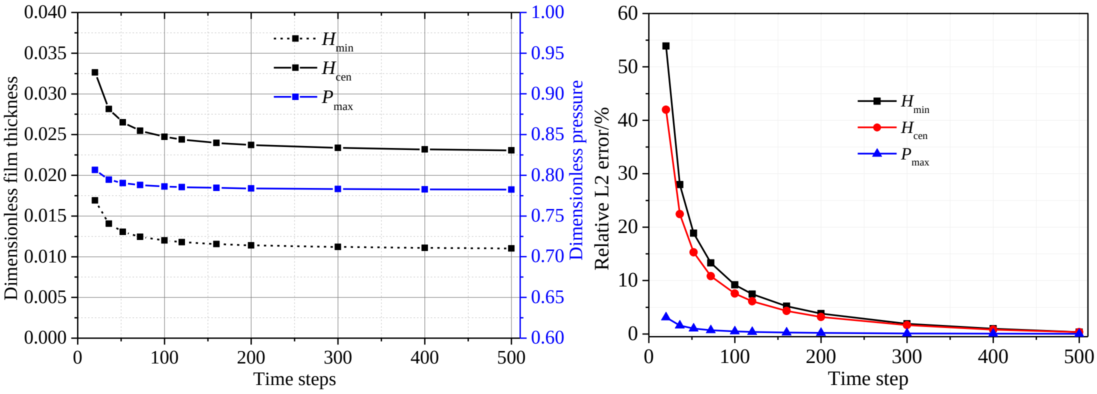

(a) t =0.5τ

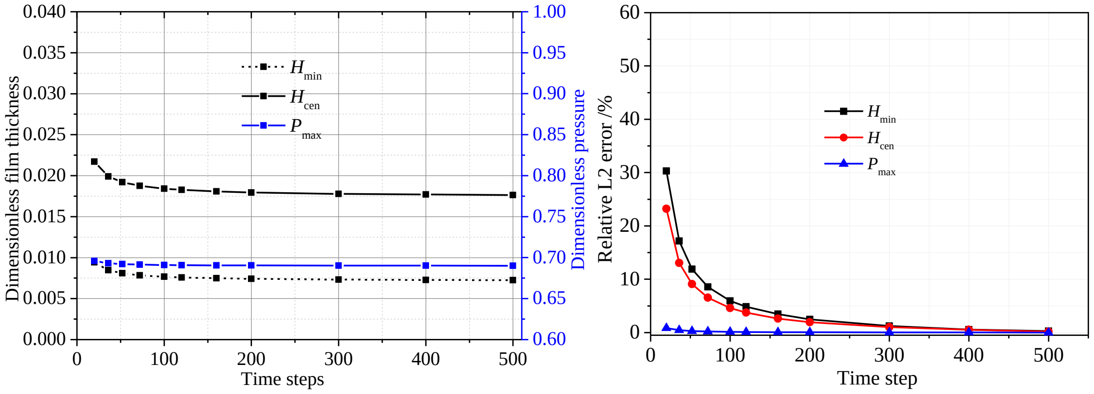

(b) t =τ

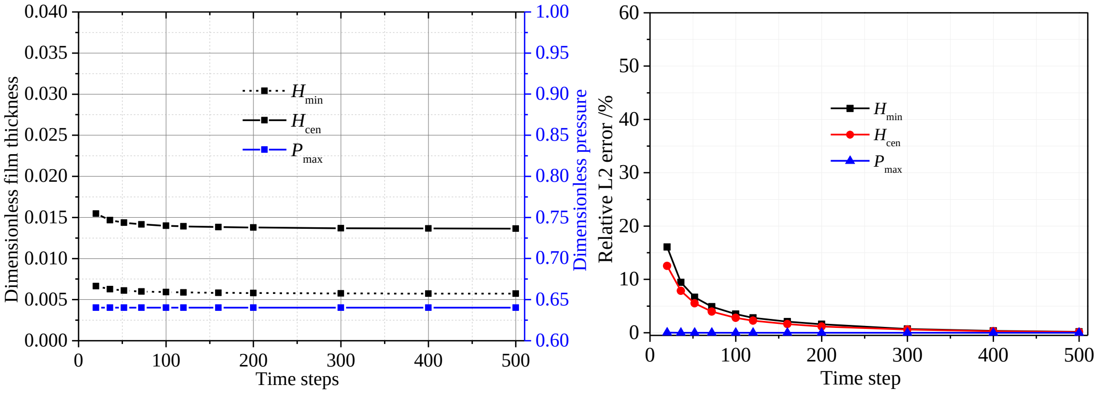

(c) t =2τ

Figure 4 The dimensionless minimum/central film thicknesses, maximum pressures and relative $L2$ errors at time instants of 0.5τ, τ and 2τ for different time step discretization of one squeeze period

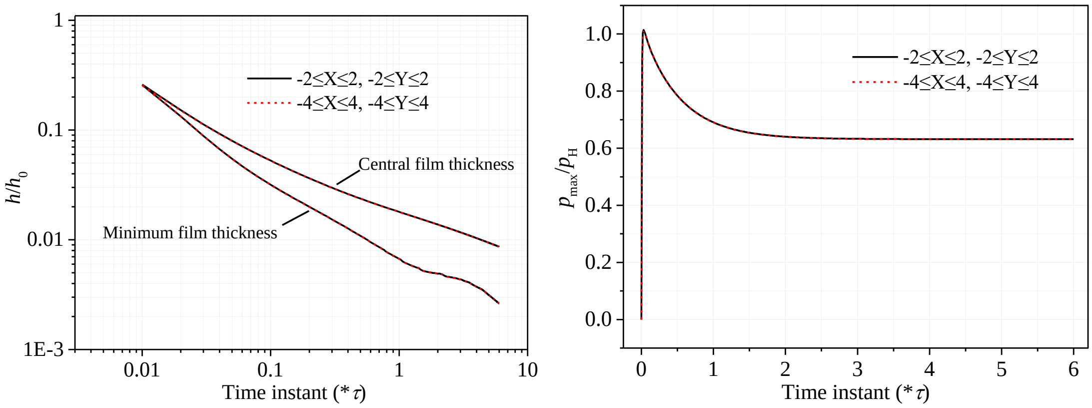

(a) (b)

Figure 5 Influence of computational domain size on minimum/central film thickness (a) and maximum pressure (b)

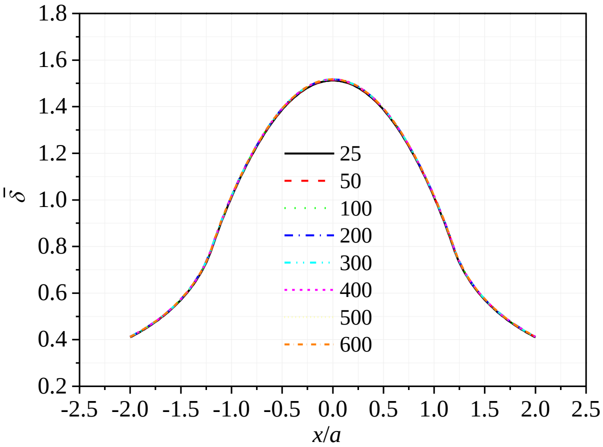

Figure 6 Influence of time step discretization on viscoelastic deformation at t=2τ

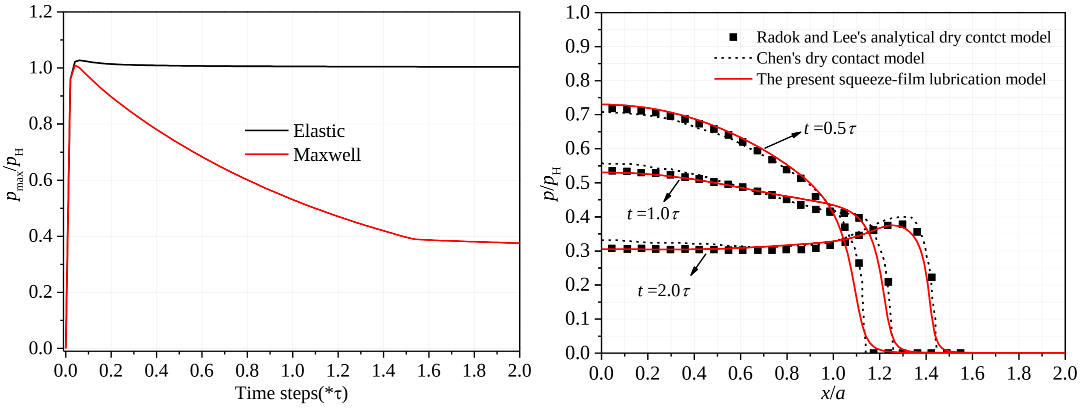

(a) (b)

Figure 7 Dimensionless maximum pressures (a) of the elastic and Maxwell models during the squeeze film processes and cross-sectional dimensionless squeeze film pressure (b) and dry contact pressure distributions

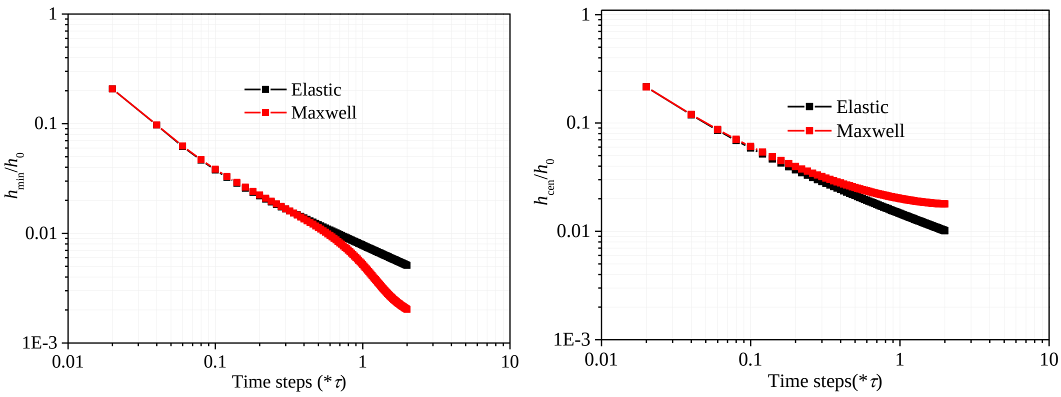

(a) (b)

Figure 8 Dimensionless minimum film thicknesses (a) and central film thicknesses (b) of the elastic and viscoelastic models during the squeeze film processes

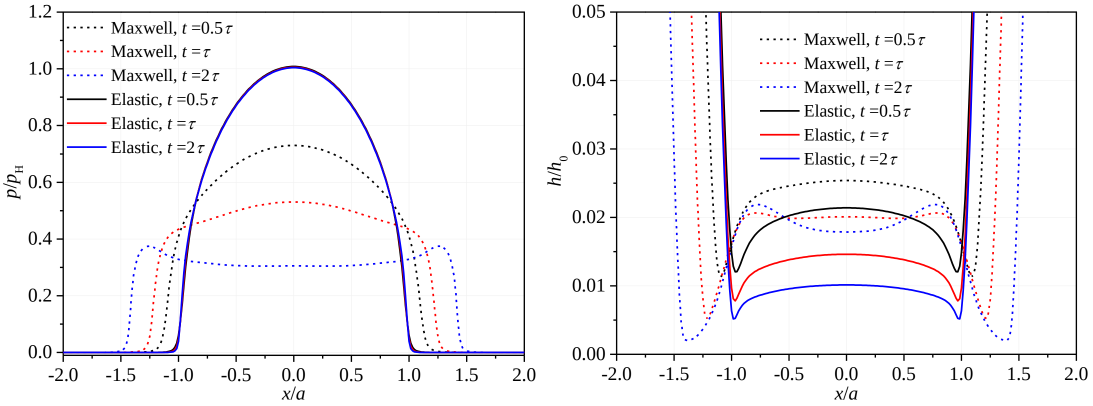

(a) (b)

Figure 9 Dimensionless pressure (p/p_{H}) and film thickness (h/h_0) distributions of y=0 along x direction at different time instants obtained by the present squeeze film lubrication model

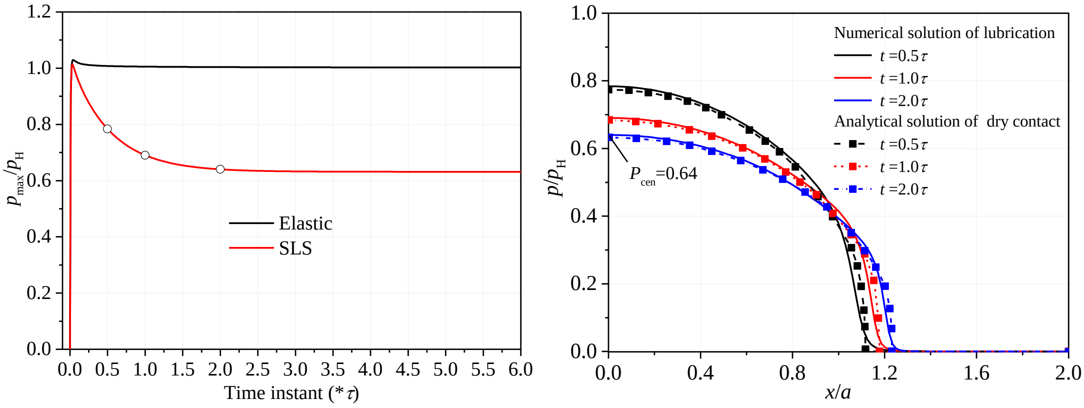

(a) (b)

Figure 10 Dimensionless maximum lubrication pressures (a) of the elastic and SLS models during the squeeze film processes and Cross-sectional dimensionless lubrication and dry contact pressure distributions (b) at several time instants (t=0.5τ, 1.0τ and 2.0τ)

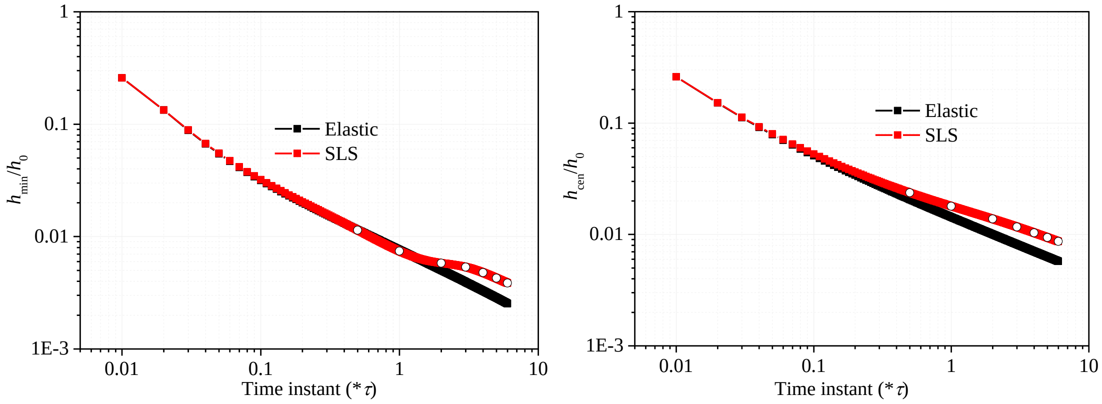

(a) (b)

Figure 11 Dimensionless minimum (a) and central film thicknesses (b) of elastic and SLS models during the squeeze film processes

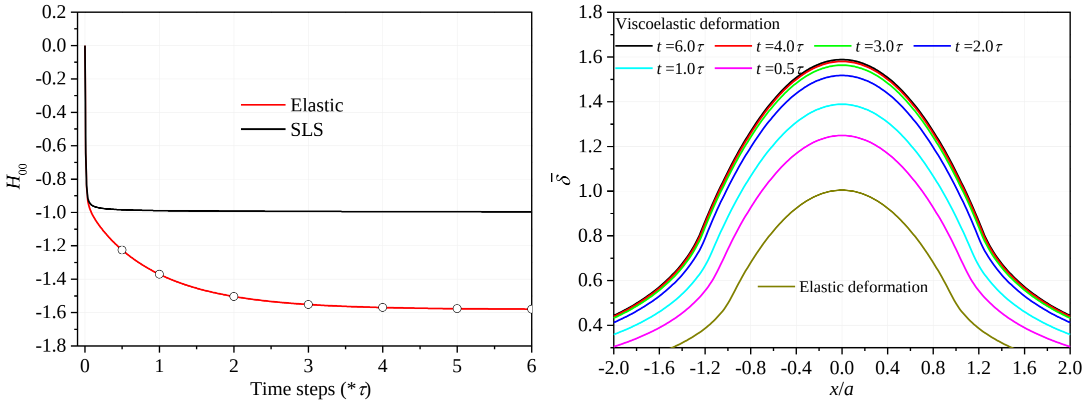

(a) (b)

Figure 12 Rigid displacements (a) of elastic and SLS models during the squeeze film processes and dimensionless elastic and viscoelastic cross-sectional deformations (b) at different time instants

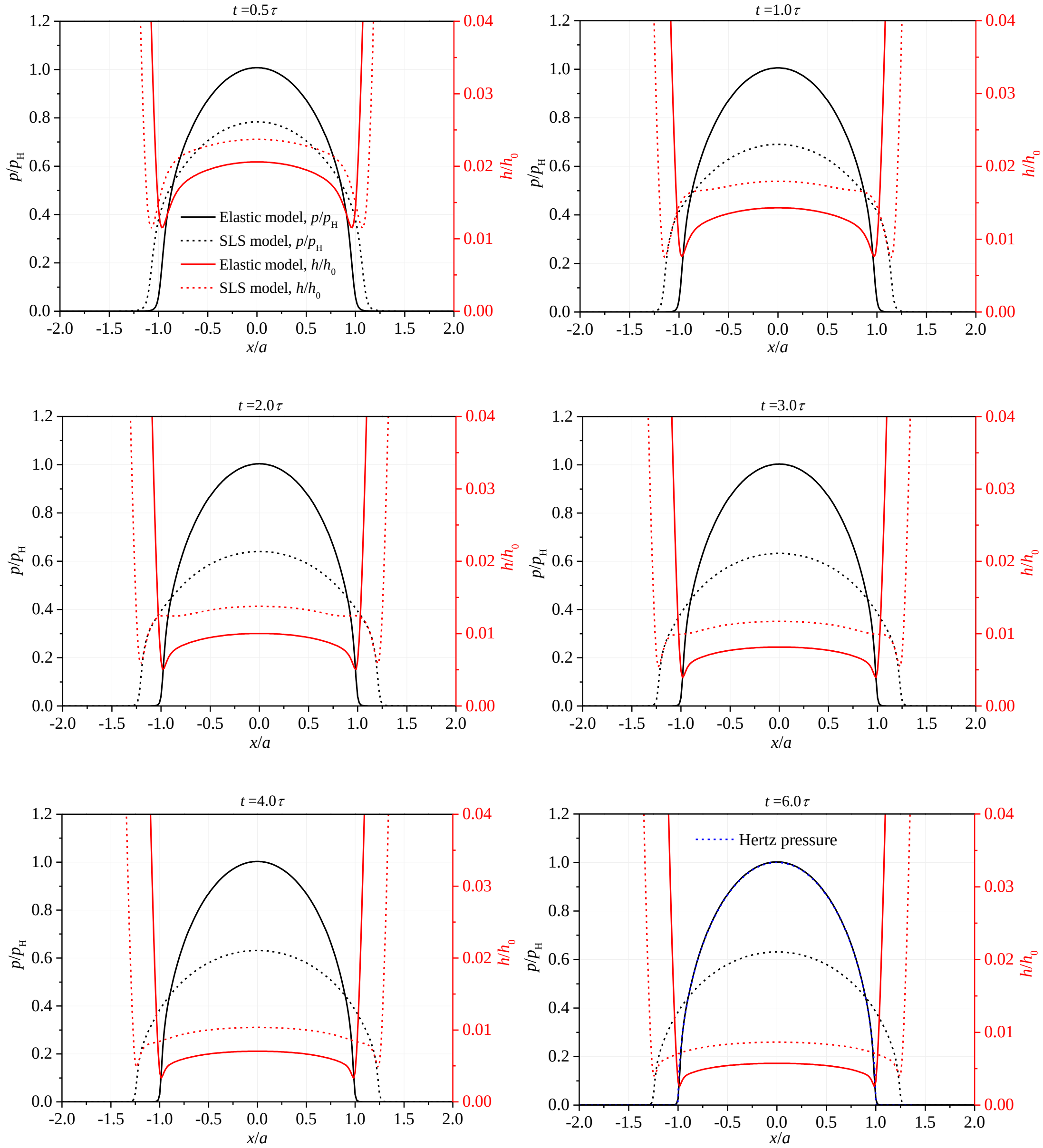

Figure 13 Cross-sectional dimensionless pressure p/p_H (*black lines*) and film thickness h/h_0 (*red lines*) distributions of y=0 along x direction of elastic and SLS models at different time steps obtained by the present squeeze film lubrication model. Dotted lines refers to the SLS model, solid lines refer the elastic case

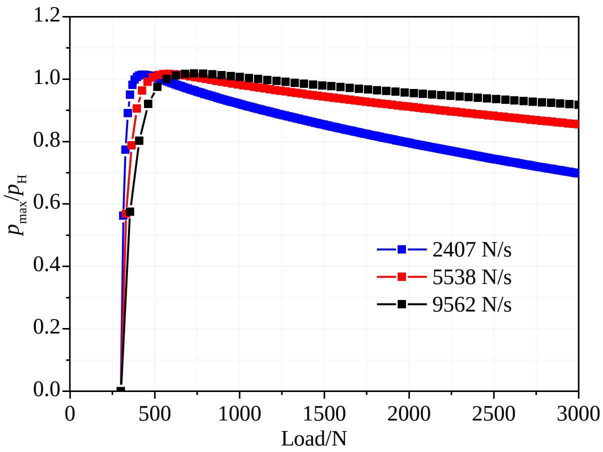

Figure 14 Dimensionless maximum pressure variations over external loads of UHMWPE hip joints for the investigated three loading rates

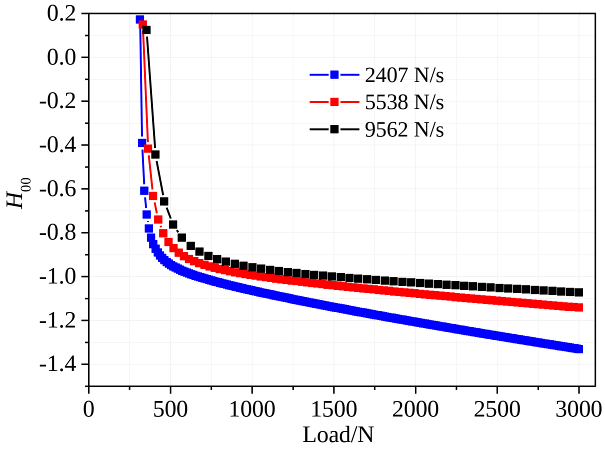

Figure 15 Dimensionless rigid displacement variations over external loads of UHMWPE hip joints at different loading rates

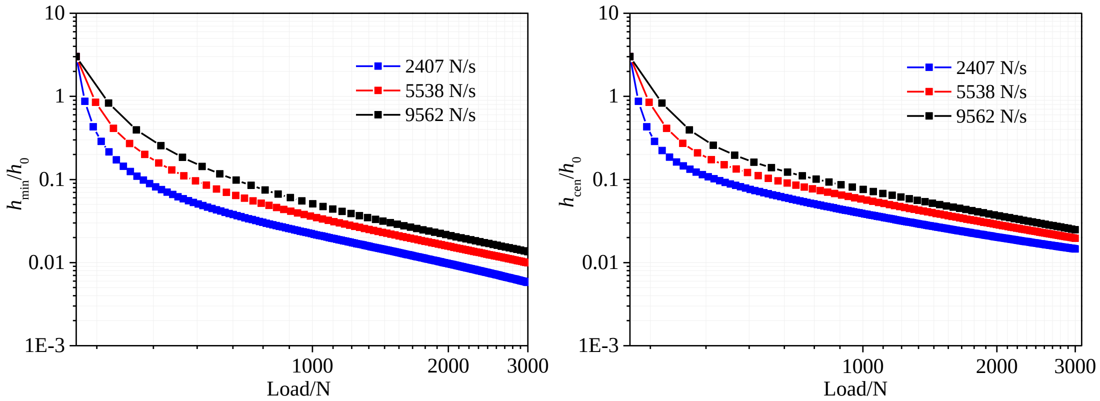

(a) (b)

Figure 16 Dimensionless minimum (a) and central film thickness (b) variations over external loads of UHMWPE hip joints at different loading rates

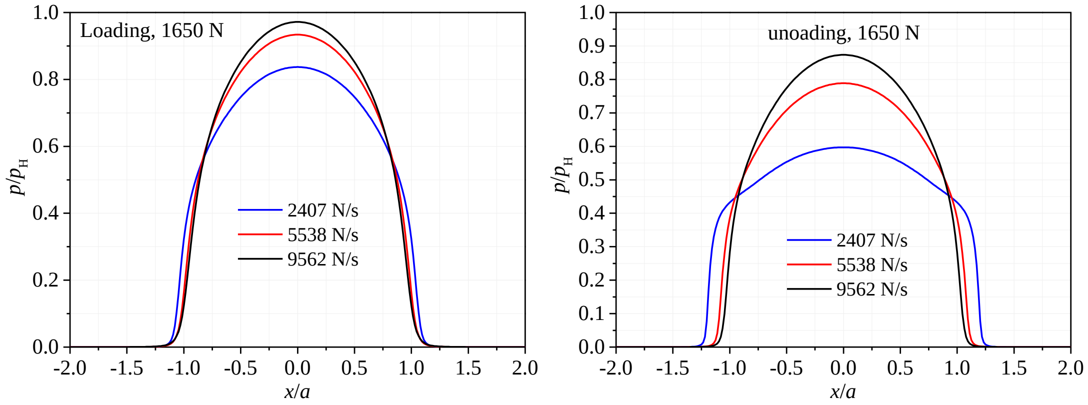

(a) (b)

Figure 17 Cross-sectional dimensionless pressure distributions along x direction when the load is 1650 N during the loading (a) and unloading (b) phases at different loading rates

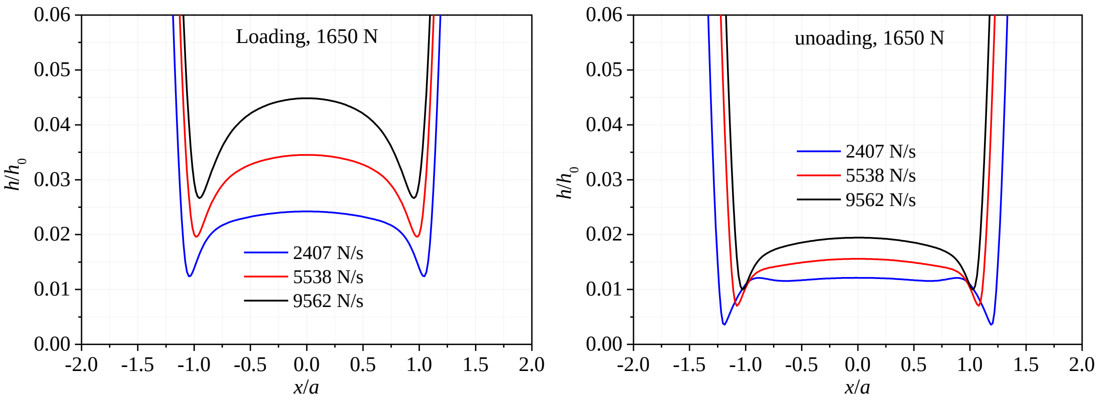

(a) (b)

Figure 18 Cross-sectional dimensionless film thickness distributions along *x* direction when the load is 1650 N during the loading (a) and unloading (b) phases at different loading rates

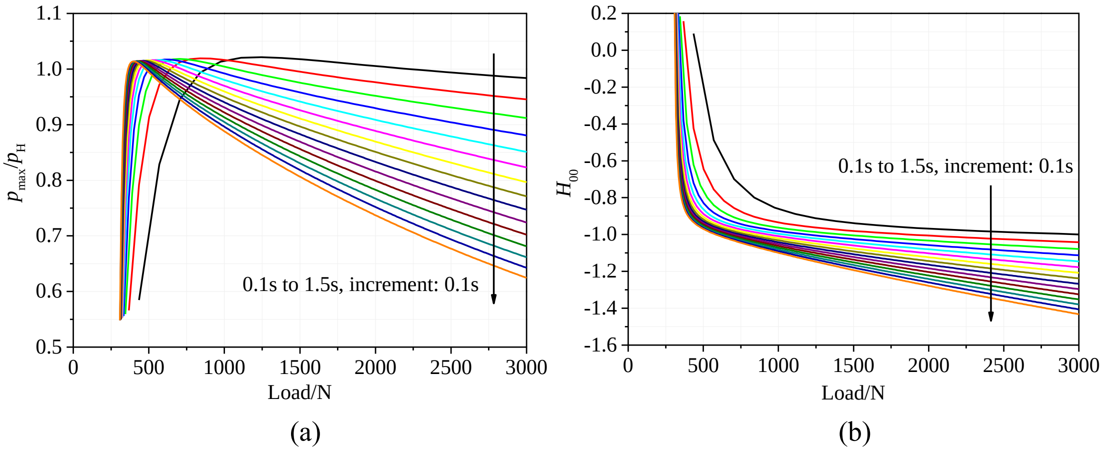

Figure 19 Dimensionless maximum pressure (a) and rigid displacement (b) variations over loads under different loading periods (0.1s to 1.5s)

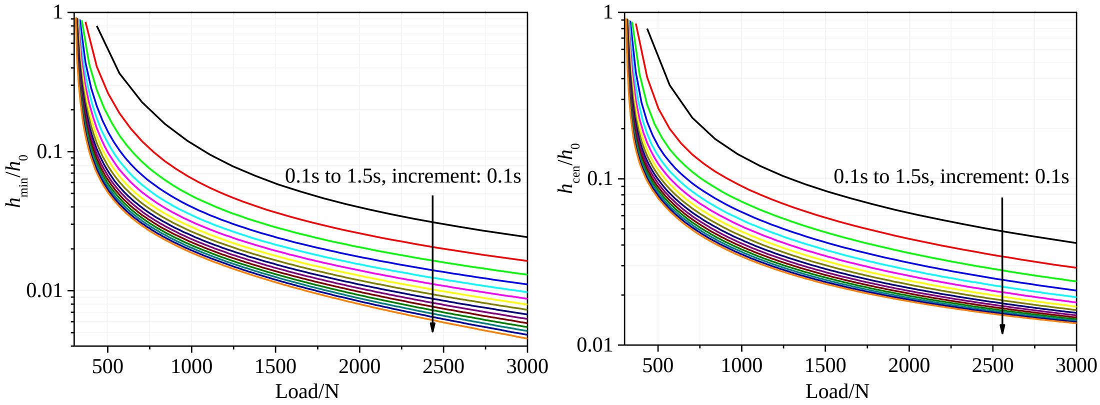

(a) (b)

Figure 20 Dimensionless minimum (a) and central film thickness (b) variations over load under different loading periods (0.1s to 1.5s)